Matter

CellPress

Article

# *para*-Aramid Fiber Sheets for Simultaneous Mechanical and Thermal Protection in Extreme Environments

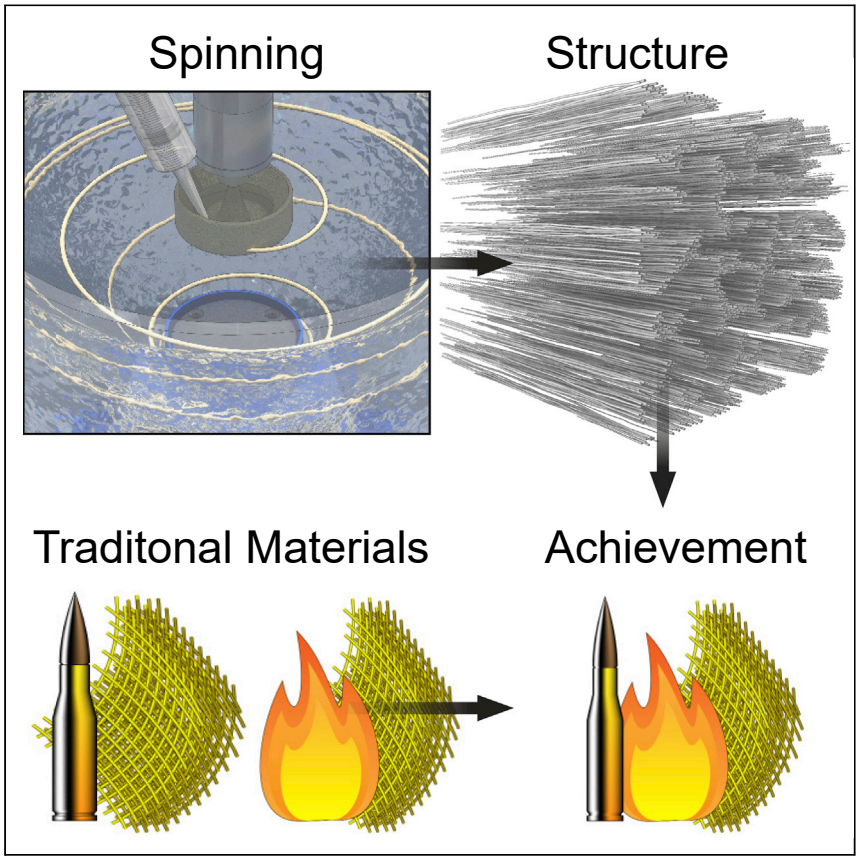


Grant M. Gonzalez, Janet Ward, John Song, ..., John F. Zimmerman, F. John Burpo, Kevin Kit Parker

kkparker@g.harvard.edu

HIGHLIGHTS

Demonstrated a multifunctional, protective material for military personnel

Fabricated a non-woven fabric with ballistic and thermal protective properties

Used structure-function relationships to improve material performance

Overcame traditional trade-offs between protective materials

First responders and military personnel require protection against multiple hazards. However, the structure of conventional materials only provides protection against a single threat. By combining a porous network with aligned fibers, this work demonstrates a multifunctional material with a high insulation and high ballistic resistance. Overcoming the limitations of conventional materials, this approach enables simultaneous thermal insulation and mechanical protection, serving as an ideal material platform for the design of high-performance protective equipment for aerospace and warfare applications.

4 **Demonstrate**
Proof-of-concept of performance with intended application/response

Gonzalez et al., Matter *3*, 742–758
September 2, 2020 
https://doi.org/10.1016/j.matt.2020.06.001

CellPress

Matter

Article

# *para*-Aramid Fiber Sheets for Simultaneous Mechanical and Thermal Protection in Extreme Environments

Grant M. Gonzalez,[1] Janet Ward,[2] John Song,[2] Kathleen Swana,[2] Stephen A. Fossey,[2] Jesse L. Palmer,[3] Felita W. Zhang,[3] Veronica M. Lucian,[3] Luca Cera,[1] John F. Zimmerman,[1] F. John Burpo,[3] and Kevin Kit Parker[1,3,4,*]

## SUMMARY

**Personnel operating in extreme environments require equipment that protects against multiple hazards. Currently, protection against both thermal and ballistic threats requires the combination of multiple high-performance materials that increases equipment weight and complexity. Here, we hypothesized we could achieve simultaneous protection by manufacturing a porous network of aligned fibers, combining the mechanical properties of continuous fibers with the thermal properties of porous aerogels. Choosing *para*-aramid polymers as the building block, we engineered precursor solutions to be fluid-like during fiber spinning and solid-like during fiber formation. This allowed for the fabrication of porous, continuous *para*-aramid fiber sheets (*p*AFS) with fiber diameters an order of magnitude lower than that of commercial *para*-aramid fibers. Although exhibiting moderately reduced single-fiber mechanics, these *p*AFS had fragment projectile resistance comparable with commercial *para*-aramids, while providing 20-fols heat-insulation capability. With these synergistic properties, the nanofiber sheets act as a multifunctional material that can provide improved simultaneous protection.**

## INTRODUCTION

The extreme environment of outer space offers multiple threats that require personal protection. To provide protection from space debris and solar radiation, Apollo-era astronauts utilized moon suits composed of multiple materials including Kevlar and Nomex.[1,2] Kevlar exhibits high mechanical ultimate tensile strength and modulus, providing ballistic and fragmentation protection.[3,4] Nomex provides minimal ballistic protection but offers high thermal resistance, insulating astronauts from the extreme temperature differentials in space.[5–7] While multiple-layer construction serves to protect against multiple threats, if protective equipment could be manufactured from a single multifunctional material it could potentially reduce both carrying weight and fabrication complexity. In practice this can be difficult to achieve, as the traditional mechanisms for thermal insulation and mechanical energy dissipation are in direct competition with one another.[8–10] To achieve the next generation of high-performance fibers, a combination of material structures is needed to break this fundamental paradigm in functionality.

The mechanical performance of Kevlar and thermal properties of Nomex provide design criteria for multifunctional materials with high thermal resistance and ballistic

### Progress and Potential

First responders and military personnel working under extreme conditions require protection against multiple hazards, including thermal and ballistic protection. However, traditional materials lack multiple types of protection in a single protective layer. By controlling the chemical and structural makeup of high-performance fibers across multiple length scales, this work demonstrates a multifunctional sheet capable of providing simultaneous thermal and ballistic protection. These sheets are composed of long, continuous fibers to resist a mechanical load and large pores to limit heat transfer. By combining these structure-function properties, these fibers overcome traditional trade-offs, providing mechanical performance equivalent to commercially available ballistic fibers while providing 20-fold insulation capability. Overcoming previous limitations, this approach enables simultaneous thermal and mechanical protection for astronauts, bomb disposal experts, and warfighters.

protection. The high modulus and strength of Kevlar result from its *para*-aramid rigid rod polymer backbone that forms from liquid crystal solutions with ordered domains that spontaneously align and crystallize under the shear stress of fiber spinning.[3,4] The thermal insulation of Nomex derives from its *meta*-aramid, kinked polymer backbone that inhibits polymer packing and results in slow phonon heat transport along unordered bonds throughout the fiber.[6] Due to the polymer packing difference of these aramid materials, each material trades off between thermal and mechanical protection[11] by orders of magnitude. Recently, the development of chemically breaking Kevlar into nanoscale building blocks has enabled the altering of this basic aramid material structure-function relationship,[12–14] allowing fibers and their aligned crystallites to be dispersed into randomly aligned films. The fabrication of these building blocks has enabled research toward multifunctional materials including *para*-aramid infrared stealth films and aerogel threads with mechanical properties higher than those of traditional heat-insulation materials.[15] The aerogel threads, for example, use a porous network of nanofibrils allowing for thermal insulation while the thread helps to bear the mechanical load.[16] However, these aramid building blocks rely on the degradation of the *para*-aromatic system and the formation of fibrils instead of continuous fibers. With structural degradation at the polymer and fiber spatial scales compared with commercial *para*-aramids,[17,18] these aramid materials exhibit lower modulus and ultimate tensile strengths (10 MPa and 3 MPa, respectively),[16] lacking the high mechanical performance of traditional Kevlar and Twaron *para*-aramid fibers (160 GPa modulus and 5 GPa ultimate tensile strength). As a result, there is still a need to produce continuous *para*-aramid fibers to recover these mechanical properties for multifunctional performance.

To attain a unique combination of material properties for a wide range of applications, recent research has shown that traditional structure-function relationships can be combined at multiple length scales to promote multifunctionality.[16,19–21] For *para*-aramid materials to achieve greater simultaneous thermal and mechanical performance,[16] this paper aims to advance the work on *para*-aramid aerogels by aligning fibers within the aerogel along the direction of mechanical load as in commercial Kevlar or Twaron. Specifically, we hypothesized that an aligned continuous network of non-woven *para*-aramid fibers would be capable of bearing mechanical loads, while the porous networks would limit heat diffusion without compromising structural function. Collectively, this would allow *para*-aramid fibers to overcome these traditional structure-function limitations, enabling truly multifunctional materials. To fabricate *para*-aramid fiber sheets (*p*AFS), we used the immersion Rotary Jet-Spinning platform (iRJS).[22] To ensure the continuous fiber formation for a scale relevant to proof-of-concept testing, rheological properties of fiber precursor solutions were carefully tailored to ensure the solution to be fluid-like during spinning and solid-like during fiber formation. This allowed the fabrication of macroscopic 100-$cm^2$, 5-g sheets, which were used for fragmentation and thermal protection testing. Fragmentation testing showed that non-woven *p*AFS exhibited ballistic protection comparable with that of commercial ballistic resistant textiles. Additionally, *p*AFS showed reduced heat conductivity and 20-fold improved thermal insulation as compared with commercially available *para*-aramids. Collectively, this indicates that the method of fabricating these *p*AFS can be used to overcome traditional limitations in fiber performance, enabling multifunctional materials that can offer protection in extreme environments.

## RESULTS AND DISCUSSION

Improved design has enhanced the performance and reduced the bulkiness of protective materials utilized in extreme conditions such as an improvised explosive

[1]Disease Biophysics Group, Wyss Institute for Biologically Inspired Engineering, John A. Paulson School of Engineering and Applied Sciences, Harvard University, 29 Oxford Street, Pierce Hall 318, Cambridge, MA 02138, USA

[2]US Army Combat Capabilities Development Command Soldier Center, Natick, MA 01760, USA

[3]Department of Chemistry and Life Science, United States Military Academy, West Point, NY 10996, USA

[4]Lead Contact

*Correspondence: kkparker@g.harvard.edu

https://doi.org/10.1016/j.matt.2020.06.001

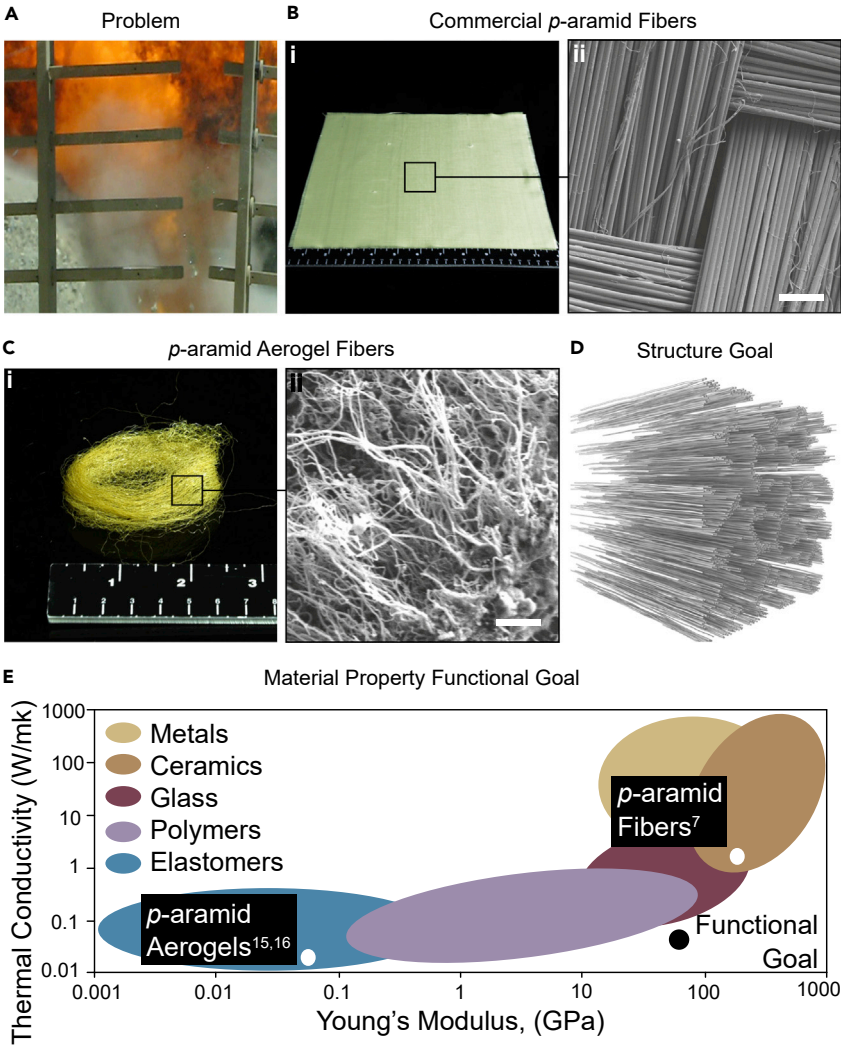


**Figure 1. Limitations in Traditional Materials**

(A) An improvised explosive device blast produces high velocity, low mass debris impacts, and heat.

(Bi and Bii) (Bi) Twaron *para*-aramid textiles with (Bii) continuous fiber weaves. Scale bar, 100 μm.

(Ci and Cii) (Ci) *para*-aramid aerogel fibers and (Cii) its porous network. Scale bar, 5 μm.

(D) This work's structural goal to achieve a material with long, continuous fibers.

(E) This work's functional goal compared with traditional materials.

device blast (Figure 1A) or space. However, there is a fundamental material property limitation between thermal insulation (inverse of thermal conductivity) and mechanical protection (Young's modulus). For example, commercial *para*-aramid ballistic resistant fibers (trade names Kevlar or Twaron, Figure 1B) provide poor thermal insulation while aramid aerogels (Figure 1C) provide thermal protection at the cost of mechanical durability. To overcome the limitations of both materials, we wanted to create a porous network of aligned, continuous fibers (Figure 1D). The continuous long fibers provide a rigid material to transmit the energy of a mechanical impact across an area larger than the initial impact site while the porosity would limit the heat transfer through the material. With this structural goal, this work aims to achieve a multifunctional material that provides thermal and mechanical protection (Figure 1E).

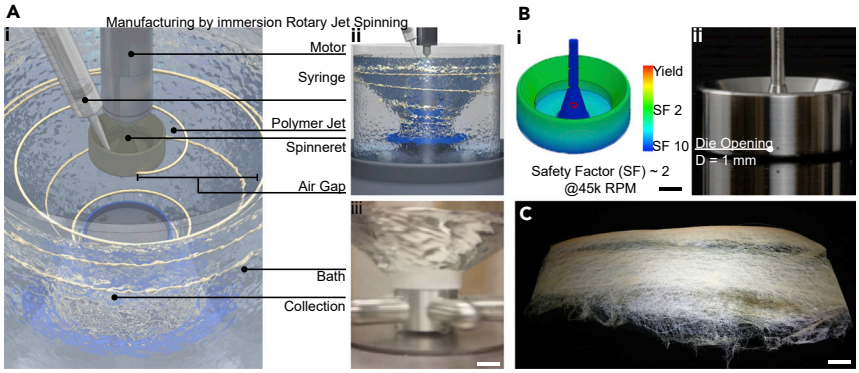


**Figure 2. Manufacturing by Immersion Rotary Jet-Spinning**

(Ai and Aii) (Ai) A computer-aided design schematic of the immersion Rotary Jet-Spinning platform (iRJS). (Aii) Side view of computer-aided design schematic. (Aiii) photo of the iRJS. Scale bar, 5 cm. (Bi and Bii) (Bi) The reservoir was simulated to have a safety of factor of 2 at 45,000 rpm. Scale bar, 1 cm. (Bii) A photo of the reservoir shows one of two 1-mm orifices. Scale bar, 70 mm. (C) Manufactured *para*-aramid fiber sheets (*p*AFS). Scale bar, 1 cm.

To fabricate the porous nanofiber sheets that provide simultaneous thermal and mechanical protection, we chose to use iRJS[22] (Figure 2A), a dry-jet wet spinning method for producing continuous fiber sheets. iRJS relies on spinning a spinneret at high speeds (>1,000 rpm) and using centrifugal forces to manufacture custom nanofibers. To produce *p*AFS, we injected poly(*para*-phenylene terephthalamide) sulfuric acid (PPTA-$H_2SO_4$) solutions into the spinneret at a continuous flow. The spinneret itself was machined out of Hastelloy 276 to ensure mechanical stability at rotation speeds and chemical compatibility with sulfuric acid (Figure 2B). Once extruded into the air gap, the polymer jet thins out before hitting a precipitating bath. Here, diffusion will drive out the sulfuric acid from the jet into the water bath, resulting in the formation of a solid fiber. The bath itself is rotating due to a stirring collector; the bath therefore pulls the fibers along the streamlines of the vortex onto the collector. During collection, the fibers interconnect to make a network. After spinning, lyophilization preserves that network, replacing water with air. Using this approach, we were able to produce thin continuous sheets of *para*-aramid fibers from 1% (wt %) solutions (Figure 2C). This suggested that iRJS could be used to form *p*AFS for ballistic testing; however, initial production was limited to 1 g of material sample, with 1-cm × 5-cm width-to-length dimensions. Additionally, initial thin sheets showed limited consistency, marking them as insufficient for ultimate ballistic and heat performance testing. This limited size and inconsistency resulted from a lack of rheological control of the precursor material.

To better control fiber production, an understanding of the viscoelastic properties of the PPTA-$H_2SO_4$ dopes during spinning as measured on a rheometer was critical (Figures 3Ai–3Aiv). To begin the spinning process, jet initiation requires the solution to be shear thinning and to exit the orifice with the smallest possible diameter, thus allowing the production of fibers with a diameter on the scale of 1 μm (Figure 3Bi). A viscosity decrease of the dope with increasing shear force ensures that the solution is shear thinning: with an increasing shear rate, the viscosity of the material decreases, thereby allowing the solution to more readily extend and narrow into a jet during spinning. Shear rates relevant to the iRJS are at a minimum 100 $s^{-1}$ and greater depending on rotation speed and die diameter. At these shear rates, the 0.5% and 1% solutions undergo shear thinning, while the 2% solution deformed and broke apart into pieces and was not stable under rheological testing (Figure 3Bii). A normal force

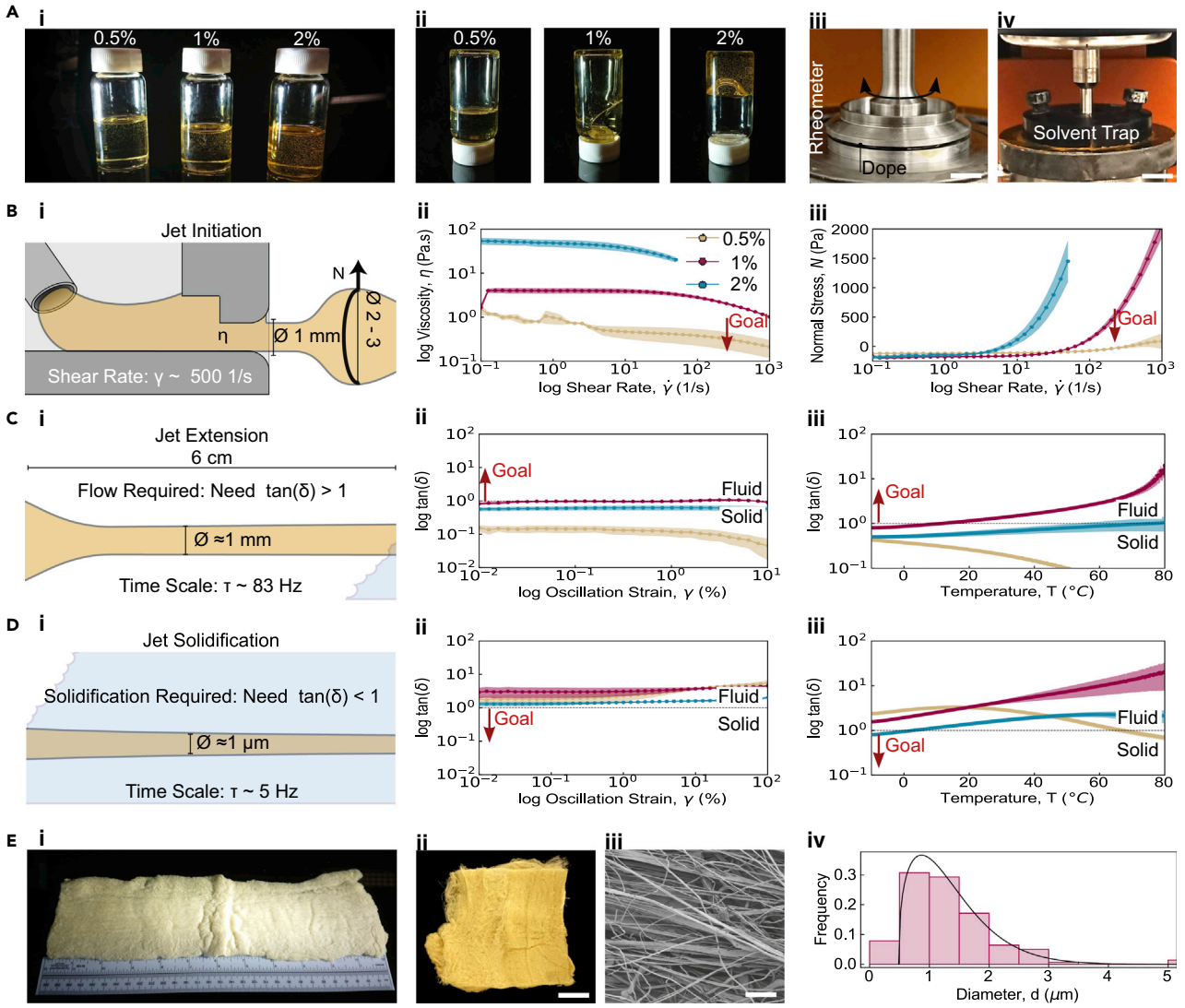


**Figure 3. Engineering Poly(*para*-Phenylene Terephthalamide) Sulfuric Acid Solutions (PPTA-$H_2SO_4$) and Rheological Properties**

(Ai–Aiv) (Ai) Solutions of 0.5%, 1%, and 2% PPTA-sulfuric acid dopes at rest and (Aii) relaxing 30 s after being flipped. (Aiii) A rheometer with a cone geometry and (Aiv) solvent trap. Scale bars, 8 mm.

(Bi–Biii) (Bi) Measured rheological properties during jet initiation are (Bii) viscosity and (Biii) normal force with shear rate.

(Ci–Ciii) (Ci) Measured rheological properties during jet extension are tan($\delta$) at 83 Hz over variable (Cii) strain and (Ciii) temperature.

(Di–Diii) (Di) Measured rheological properties during jet solidification are tan($\delta$) at 5 Hz over variable (Dii) strain and (Diii) temperature.

(Ei–Eiv) (Ei) Porous, continuous nanofiber sheets. (Eii) The sheet cut into 10 × 10-cm samples. Scale bar, 2 cm. (Eiii) SEM micrograph. Scale bar, 40 μm. (Eiv) Fiber diameter distribution (n = 3 production runs).

In (B) to (D), area fill data are presented as mean ± standard error of the mean.

generation leads to die swelling whereby the jet of a solution exiting an orifice swells to a size greater than the orifice.[23,24] The normal force generation across the surfaces adds a pressure that is released when the solution leaves the orifice. To ensure that the solution has minimal jet size after exiting the orifice, the jet needs to have a minimal normal force during spinning. While Newtonian solutions have 10% die swelling at high shear rates, viscoelastic polymer dopes may have die swelling higher than 300% and as low as 50%.[25] A high positive normal force generation leads to a high die swelling ratio while a negative normal force leads to a low die swelling ratio.[26] While increasing the spinning speed and resultant shear rate causes a decrease

in jet size during jet thinning, this growth in shear rate results in increased normal force generation (Figure 3Biii). To avoid excess die swelling, we chose 5,000 rpm rotation speed and shear rate of 500 $s^{-1}$ to thin our 1% solution into jets. While decreasing the size of the orifice will decrease the initial size of jet, decreasing the orifice will also increase the shear rate, leading to a higher normal force generation and ultimately similar fiber diameters as seen with the test spinning of non-hazardous solutions (see Figure S1).

During extension from the orifice, the solution needs to thin into a jet and as a result should be viscous dominant, similar to other fiber-spinning processes (Figure 3Ci).[27] This helps ensure continuous jet flow; however, if a solution is elastic, it would bead instead of thinning, leading to short fibrils and incomplete fibers. Furthermore, during collection, the dope needs to be elastic dominant to ensure the jet does not deform before solidifying (Figure 3Di).[27] To measure these properties, we used oscillatory shear of the rheometer to probe the material at a timescale relevant to fiber spinning (5,000 rpm, ~83 Hz) and collection (300 rpm, ~5 Hz). We reasoned that by mimicking these rotational speeds, we would apply forces to the dope comparable with those experienced during the fiber formation process. When the tangent($\delta$) (ratio of viscosity to elasticity) is greater than 1, the material is viscous dominant. Rheological testing revealed low concentration dopes (0.5%, 1%, 2%) to be elastic dominant during spinning (tan($\delta$) = 0.1, 1, and 0.9, respectively; Figure 3Cii) and viscous dominant during collection (tan($\delta$) = 2, 4, and 3, respectively; Figure 3Dii), the opposite properties as required in both cases. This trend of decreasing elasticity with longer times (lower timescale) is common among polymer dopes, whereby generally at faster time scales a polymer solution becomes more elastic dominant because the polymer chains do not have time to relax.[27] Using these solutions with these properties at room temperature therefore leads to poor fiber formation. To enable the required tan($\delta$) values for spinning and collecting, another variable needs to be examined.

Changes in temperature influence the viscoelastic properties of materials: an increase in temperature increases the movement of polymer chains, allowing for a decrease in viscosity, while a decrease in temperature limits their movement, causing a shift to elastic dominance.[27] At 83-Hz frequency relevant to spinning, the material needs to be elastic dominant. Increasing temperatures during rheometric studies from −10°C to 80°C showed an increase in tan($\delta$) for the 1% and 2% solutions (Figure 3Ciii). In this range, the 1% became viscous dominant, which occurred at temperatures 18°C or greater. This suggested a possible way forward of using heated solutions to make *p*AFS. Interestingly, the 0.5% solution does not follow the trend of the other solutions. This is likely because PPTA-$H_2SO_4$ dopes have different packing even at dilute concentrations.[28] In addition to being viscous dominant during jet formation, solutions need to be elastic dominant after jet thinning when entering the bath to ensure the formation of consistent fibers. More specifically, the jet in the bath needs to have a characteristic timescale, or the time required for the material to deform from its original shape by relaxation, that is longer than the timescale of diffusion of the sulfuric acid. As diffusion will be dependent on the ultimate size of the fibers, an elastic-dominant material during collection is preferred, as this will allow for the sulfuric acid to diffuse out before the jet collapses. Only the 2% solution became elastic dominant, which occurred at 2°C, at any temperature at a 5-Hz timescale (Figure 3Diii). However, as the solution was elastic dominant during spinning, it was not a suitable material to choose for spinning.[29] As a result, we selected the 1% solution with the smallest viscous component, as this would allow for the greatest time for solidification to occur before relaxation of the jet returned it to deflated shape.

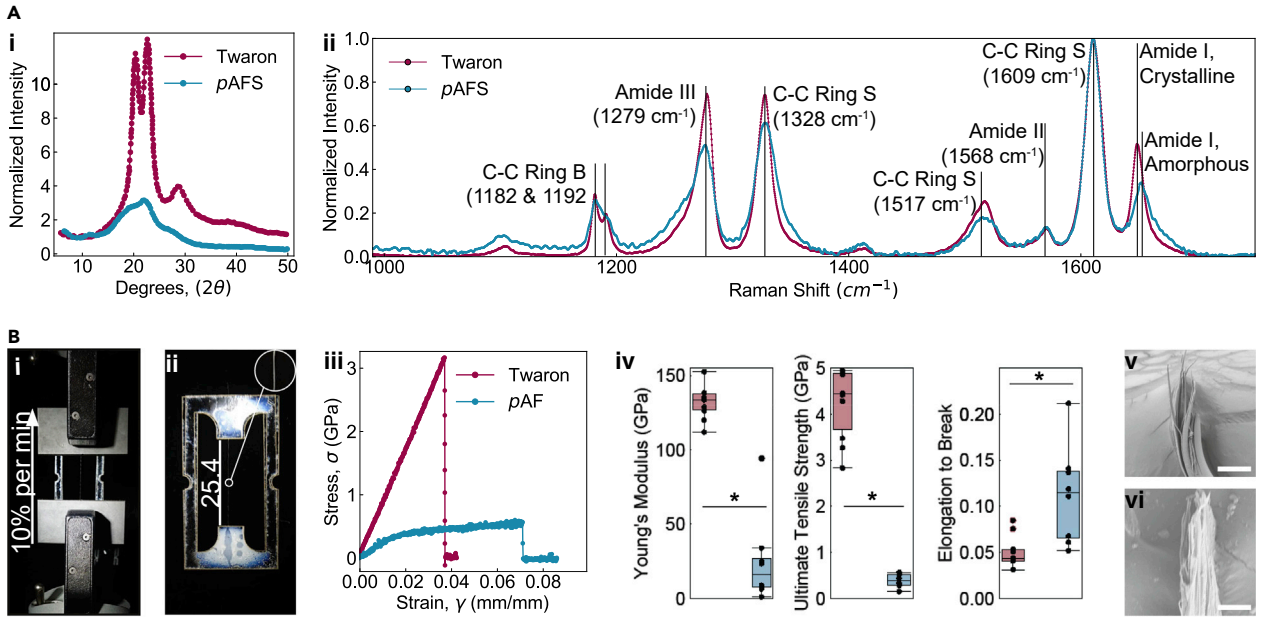


**Figure 4. *p*AFS Structure and Mechanics**

(Ai–Aii) (Ai) XRD and (Aii) polarized Raman spectra of a Twaron fiber and *p*AF (representative curve for n = 3).

(Bi–Bvi) (Bi) Single-fiber uniaxial mechanical testing of fibers until break. (Bii) A *p*AF secured to a frame. (Biii) Representative stress-strain curves and (Biv) Young's modulus, ultimate tensile stress, and elongation to break values (n = 8). Representative broken (Bv) Twaron fiber (scale bar, 10 μm) and (Bvi) *p*AF (scale bar, 2 μm). In box plots, middle line indicates the median, the upper and lower box boundaries indicate the $Q_{75}$ and $Q_{25}$ respectively, and the top and bottom whisker lines indicate M ± 1.5 IQR. Asterisk indicates a p value of <0.05.

From the rheological data, the 1% solution at ~60°C was chosen to be spun from the spinneret into a 1°C water bath. To maintain the porosity of the sheets, we froze the samples to −80°C overnight and placed them in a lyophilizer for 3 days to ensure that the water sublimed off instead of collapsing the scaffold. Following these procedures, we were able to produce fiber sheets with fiber median diameter of 1.2 μm (Figures 3Ei–3Eiv) and a density of 0.1 g $cm^{-3}$. Compared with commercial fiber with a density of 1.4 g $cm^{-3}$ and 8-μm fiber size, we observed that our fiber sheets have a greater porosity due to the lower density.

As amorphous and crystalline structures affect both mechanics and heat diffusion, we used X-ray diffraction (XRD) to quantify their crystalline-amorphous ratio. Examining the area of crystalline to amorphous peaks, the Twaron was determined to have a crystallinity of 80%, agreeing with published values.[3] The manufactured *p*AFS showed a significantly lower signal (Figure 4Ai). As amorphous content does not provide as much X-ray signal intensity compared with crystalline samples, the lower signal was attributed to being primarily amorphous. Calculating the amorphous peaks, the *p*AFS were determined to have 10% crystallinity. This low amorphous content was also confirmed by polarized Raman spectroscopy whereby the amorphous amide-II peak at 1,652 $cm^{-1}$ was dominant for the *p*AFS sample compared with the crystalline peak located at 1,648 $cm^{-1}$ of the Twaron sample (Figure 4Aii).[22,30] The *p*AFS low crystalline content was more closely related to a cast film.[16] With this structure, the *p*AFS was predicted to have a slower timescale of heat diffusion through the fiber due to its amorphous polymer packing unlike the crystalline Twaron and, therefore, limited heat conductivity.

In addition to lowering heat conduction, the amorphous content of the fiber increases elongation to break while lowering the strength and modulus of the

nanofiber compared with the commercial fiber. Using uniaxial tensile testing following ASTM D3822M-14 (Figures 4Bi and 4Bii), the changes of the mechanical properties of a single *para*-aramid fibers (*p*AF) was determined to correlate the crystallinity differences (Figures 4Biii and 4Biv). The 140-GPa modulus of the commercial fibers was 5-fold greater and its 4.5-GPa strength 10-fold greater. However, due to the amorphous content, the *p*AF had a 12%, or 4-fold greater elongation to break and plastic failure compared with the commercial Twaron. While the Twaron failed by brittle fracture between crystallites (Figure 4Bv), plastic failure was observed for the *p*AF (Figure 4Bvi).

To correlate single-fiber mechanical properties with the ballistic performance metric $V_{50}$, defined as the velocity of a projectile at which a material fails 50% of the time, we used the relation $V_{50} \sim \left(\frac{\sigma\epsilon}{2\rho}\sqrt{\frac{E}{\rho}}\right)^{1/3}$, where $\sigma$ is ultimate tensile strength, $\epsilon$ is elongation to break, $\rho$ is the density, and $E$ is the modulus of the fiber.[31] With this relation and the experimental mechanical properties of the fibers, the ballistic performance of the Twaron fibers was predicted to be only 2.4-fold greater than the *p*AFS. As a result, the fiber sheets were predicted to provide slightly less fragmentation protection while increasing heat protection.

To verify the prediction of the mechanical testing, we performed $V_{50}$ fragment simulant testing to quantify the fragmentation protection of the sheets. To test the $V_{50}$ rating, we used the US Army Combat Capabilities Development Command Soldier Center experimental setup (Figures 5Ai and 5Aii) to accelerate a skirted 17-grain (1.1 g) 0.22-caliber fragment-simulating projectile (FSP) (Figure 5Aiii) toward the material using a controllable helium gas pressure source that directly changed the resultant launching velocity. The effectiveness of the material's protection was determined by measuring the striking and residual velocity of the projectile before and after hitting the material. A registered residual velocity means complete penetration for that striking velocity while a reading of no residual velocity means the fragment was completely stopped by the material or had too low a velocity to register. Visual inspection was used to verify whether the fragment was completely stopped or had partial penetration (Figure 5B). To fairly compare the unidirectionality of our sheets versus the bidirectionality of the control commercial woven fabrics, we sandwiched the *p*AFS between two Twaron 750D woven piles. In addition to providing a more objective comparison, this material sandwich would more likely mimic a final layered composite product, as non-woven fibers are generally used as insulation and not as structural background for clothing. Furthermore, ballistic resistant *para*-aramid textiles are placed within woven sheaths in final products. As this work aims to reduce the need for multiple materials in providing ballistic and thermal protection, this experimental setup allowed for the control of differences in the two fiber materials in question. To test whether our fibers provided ballistic protection, we cross-piled nanofiber sheets in a 0° and 90° multi-ply layers in one, two, or three layers between the woven textiles. After testing, the samples were visually inspected to confirm whether there was partial penetration or complete penetration and to find out how the energy wave of the impact propagated across the sample (Figure 5B). Quantitatively, increasing the layers of *p*AFS increased the ballistic performance of the sandwich construct from 525 ft $s^{-1}$ to 657 ft $s^{-1}$ in $V_{50}$ (Figure 5Ci). While the 675 ft $s^{-1}$ $V_{50}$ of the three layers of *p*AFS placed between two layers of Twaron was smaller compared with 788 ft $s^{-1}$ $V_{50}$ of five layers of Twaron at similar densities, the values were not statistically different ($p \geq 0.151$). Replacement of one, two, or three layers from a stack of Twaron with *p*AFS resulted in no difference in ballistic resistance.

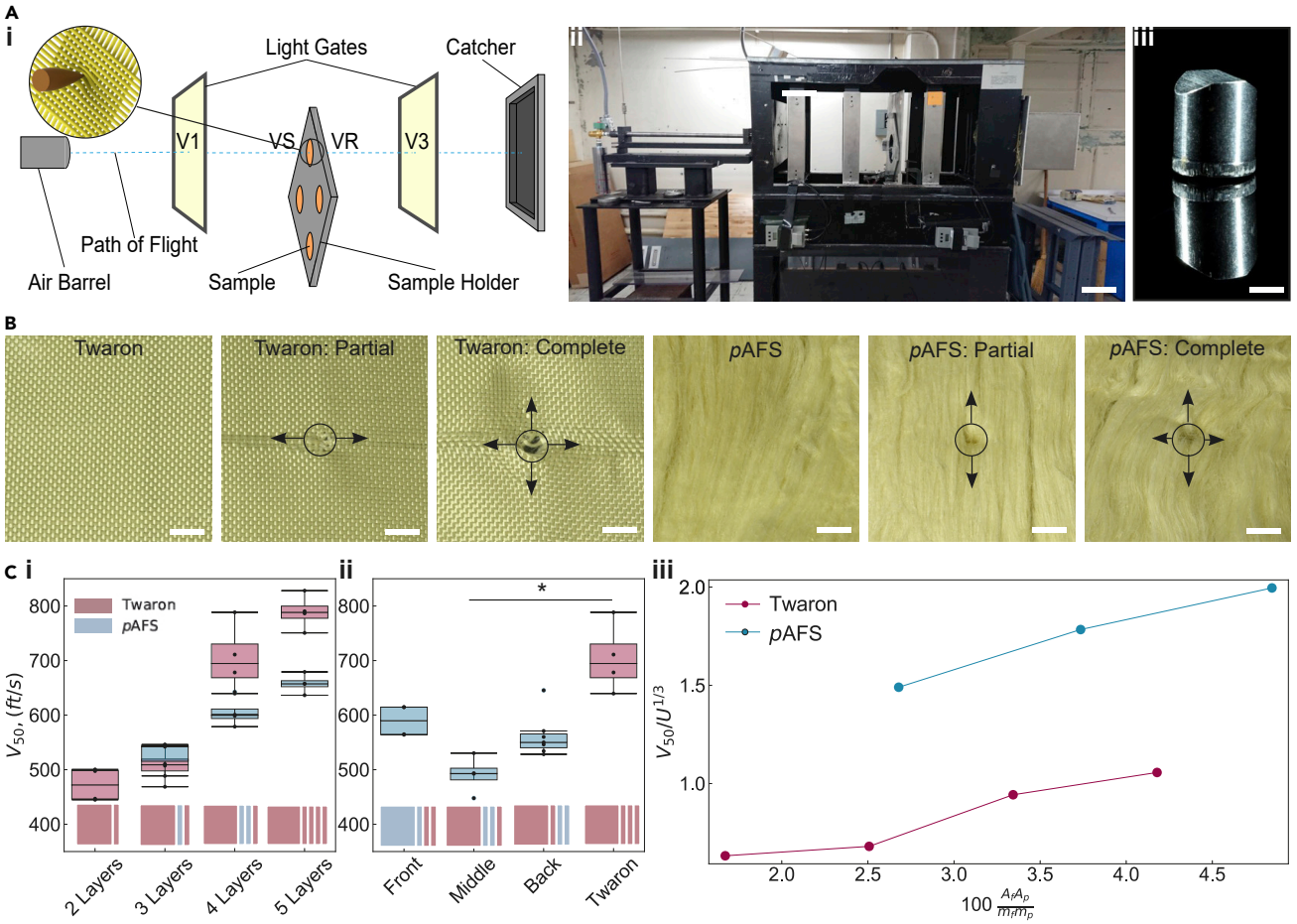


**Figure 5. Ballistic Protection of *p*AFS**

(Ai–B) (Ai) Mechanical protection against fragmentation impact testing using a fragment-simulating projectile (FSP). (Aii) A photo of the setup (scale bar, 0.5 m) and (Aiii) FSP (scale bar, 2 mm). (B) Images of control Twaron and *p*AFS before testing, after testing with a partial penetration, and after testing with complete penetration; arrows indicate energy wave propagation, Scale bars, 2 cm.

(Ci–Ciii) (Ci) Ballistic testing data of *p*AFS with increasing layers. (Cii) Ballistic testing of *p*AFS dependent on position. "Front," "middle," and "back" refer to the position of the *p*AFS layers in relation to the Twaron layers when facing the projectile (n = 4). (Ciii) Normalized $V_{50}$ data with the predicted ballistic performance (lines are plotted for visual aid). In box plots, middle line indicates the median, the upper and lower box boundaries indicate the $Q_{75}$ and $Q_{25}$ respectively, and the top and bottom whisker lines indicate M $\pm$ 1.5 IQR. Asterisk indicates a p value of <0.05.

To further examine the mechanism of protection provided by the *p*AFS, we altered the placement of two layers of *p*AFS in relation to two layers of Twaron (Figure 5Cii). Depending on their position relative to the impact site, non-woven ballistic materials can provide protection by two mechanisms: (1) as the first material interacting with the projectile, they could increase the effective area of the FSP by projecting a greater area to subsequent layers; or (2) as the last layer interacting with the impact, they could act as a mechanism for energy absorption. The effect of presenting greater projectile area is greatest when the fibers are placed in the front, and energy absorption is most prominent when the fibers are placed in the rear of the construct. Testing the sheets in each of these configurations (Figure 5Cii) had a non-statistically significant difference to conclude by what mechanism the nanofiber sheets provided protection ($p \geq 0.121$). Only the *p*AFS layered in the middle of two Twaron sheets had a statistical difference compared with four layers of Twaron ($p = 0.002$). The configuration of testing, therefore, did not affect the ballistic performance of the materials and the *p*AFS do not necessarily need to be in a sandwich configuration to provide ballistic protection. Overall, this

experimental setup allowed us to control for differences in woven versus non-woven structures and achieve an understanding of the fundamental performance of the material and not its configuration. To normalize the $V_{50}$ data to its predicted ballistic performance value based on mechanical properties, we used the equation $U^{1/3} \sim \frac{\sigma\epsilon}{2\rho}\sqrt{\frac{E}{\rho}}$, where $\sigma$ is ultimate tensile strength, $\epsilon$ is elongation to break, $\rho$ is the density, and $E$ is the modulus of the fiber.[31] This normalization reveals that the *p*AFS and the Twaron construct outperform the predicted performance of the construct based only on fiber mechanical properties (Figure 5Ciii). The porous network therefore may be providing a means of absorbing the mechanical impact in addition to potentially providing greater puncture resistance (see Figure S2).

While the $V_{50}$ of *p*AFS was slightly lower compared with commercial Twaron, the *p*AFS had improved heat insulation. To measure the heat insulation, we used a 600-W heat source and probes to measure the temperature on both sides of one layer of the nanofiber sheet and control (Figures 6A and 6B). Upon heating, the nanofiber sheets heated slower than the commercial fibers (Figure 6C). Using this setup, the heat conductivity $k$ was determined by $k = \frac{QL}{A\Delta T}$, where $A$ is the area of the sample, $Q$ is the heat flux through the sample, and $L$ is the length of the sample.[16] The heat conductivity for the *p*AFS was $1.601 \pm 0.0248$ W mK$^{-1}$ (mean $\pm$ standard error of the mean, n = 6) while that of the commercial Twaron weaves was $5.808 \pm 0.0896$ W mK$^{-1}$ (mean $\pm$ standard error of the mean, n = 3), resulting a statistically significant difference (p = 0.024). As the *p*AFS created using the methods described above are less dense and thicker, this led to an insulation value, $R$, 20-fold higher than the commercial fibers as defined by $R = \frac{L}{k}$. As the materials have an inherent different structure-function relationship and resulting thickness, accounting for these differences requires simulation heat transfer through these materials. Using material parameters based on experiments and literature, the insulation performance was simulated at a thickness of the *p*AFS at 1.75 cm (Figures 6D, 6E, and S3) and the thickness of the Twaron at 0.1 cm (Figure S4). For each thickness, the *p*AFS kept the heat sink at the lowest temperature at all time points, outperforming the air and Twaron insulating layers. Interestingly, the Twaron insulation led to a higher temperature in the heat sink compared with an insulating layer of air due to its higher thermal conductivity under radiative heat transfer.

As a proof-of-concept demonstration when exposed to protection from extreme heat, a blowtorch with a radiative heating element attached was used melt a gelatin astronaut figurine without a textile covering, with a control Twaron protective covering, and with the nanofiber sheets protective covering (Figures 6F–6H; Videos S1, S2, and S3). As air is an excellent insulator with a thermal conductivity of 0.026 W (m$^2$ K)$^{-1}$,[32] the blowtorch was placed as close to the nearest material as possible without causing material ignition. Therefore, the torch placement without a protective layer demonstrates the heat going into the system and not as a control for the thermal insulation properties of air. To account for the difference in distance between the air and Twaron cases, we used an insulation simulation to confirm the timescale of melting of the air-only experimental factor (Figure S5).

Without any protection, the astronaut melted within 5 min (Figure 6F and Video S1) and with the Twaron protection within 17 min (Figure 6G and Video S2). When exposed to heat with the nanofiber sheet protection, however, the astronaut remained unmelted after 30 min (Figure 6H and Video S3), indicating its potential to act as a multifunctional material with both fragmentation and thermal protection in extreme environments. This multifunctional benefit resulted from the construction of a multistructured material. The long, continuous fibers with relatively high mechanical properties compared with thermally insulative fibers provided the structure

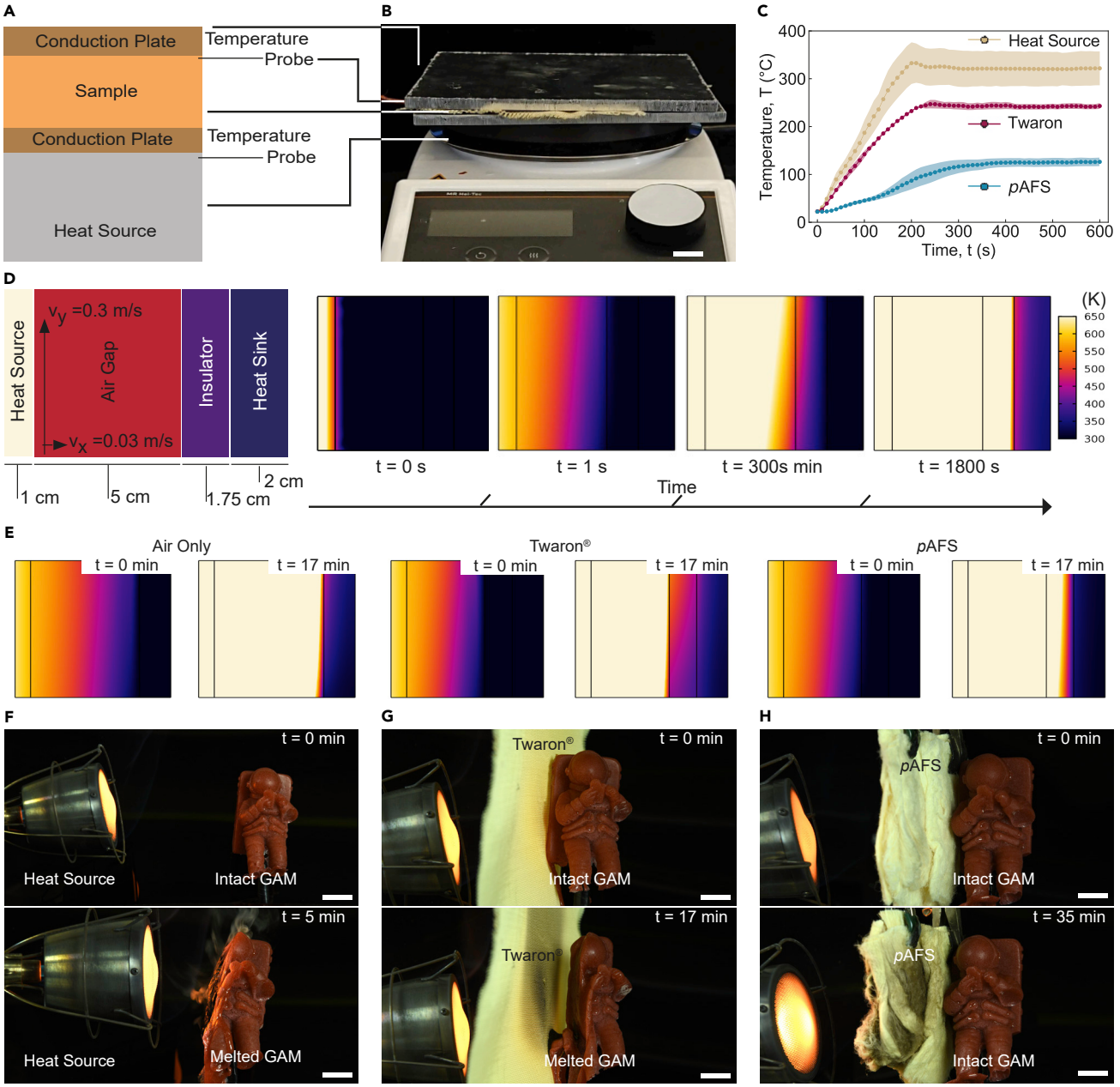


**Figure 6. Thermal Protection**

(A–C) Heat conductivity (A) schematic and (B) setup consisting of a hot plate, temperature probes, and sample (scale bar, 2 cm) used to measure the (C) temperature between both sides of a sample (representative curves for n = at least 3; area fill data are presented as mean ± standard error of the mean). (D–H) (D) Insulation performance was simulated over time for (E) air as an insulator, Twaron as an insulator, and *p*AFS as an insulator. Flame testing with (F) no material, (G) Twaron sheet, and (H) *p*AFS were tested by measuring the time for a gelatin astronaut model (GAM) to melt when exposed to a blowtorch (n = 1). Scale bars, 2 cm.

to bear a mechanical load while the decreased fiber size allowed for the fibers to be freestanding in a porous network, allowing for improved heat insulation.

## Conclusions

Materials traditionally provide mechanical or thermal protection because their structure-function relationships are mutually exclusive. By combining the structure of

commercial continuous fibers with the porosity of aerogels, flexible *p*AFS were prepared to overcome these limitations in traditional materials manufacture. *p*AFS were engineered by controlling the precursor solution to be viscous dominant during spinning and elastic dominant during fiber formation and collection in the iRJS system. This enabled iRJS production of continuous fibers with subsequent lyophilization, forming a porous network with low heat conductivity. Future work will further improve the ballistic performance of the *p*AFS against high-velocity rounds by spinning fibers from liquid crystalline solutions. As a proof of concept, this work spun fibers from dilute, isotropic solutions that do not readily crystallize. The spun fibers therefore had greater amorphous content and elongation to break, but lower modulus and ultimate tensile strength compared with Twaron fibers. Spinning these fiber sheets from liquid crystalline solution will increase mechanics while only slightly decreasing heat-insulation capabilities. In addition, further decreases in fiber diameter will further increase the heat insulation of the sheet by increasing the effective porosity to that of current aerogels. Eventually, this methodology will extend the protective thermal and mechanical capabilities to include that of commercial Twaron and high-performance aerogels in one material.

## EXPERIMENTAL PROCEDURES

### Resource Availability

#### *Lead Contact*

Further information and requests for resources should be directed to and will be fulfilled by the Lead Contact, Prof. Kevin Kit Parker (kkparker@g.harvard.edu).

#### *Materials Availability*

This study did not generate new unique reagents.

#### *Data and Code Availability*

The COMSOL thermal simulation code generated during this study are available at Mendeley Data: https://doi.org/10.17632/xxrgfryrwj.1.

### *para*-Aramid Dope Preparation

With mechanical stirring (300 rpm) and under a nitrogen environment, poly(*para*-phenylene terephthalamide) (Fiber Glast 554 Kevlar Pulp) was dissolved in sulfuric acid (Sigma-Aldrich 258105-2.5L) to create poly(*para*-phenylene terephthalamide) and sulfuric acid (PPTA-$H_2SO_4$) solutions in a 500-mL reaction vessel for 90 min at 85°C. Nitrogen was used to displace oxygen, which can lead to sulfuric acid degrading the polymer via oxidation. The solute and solvent were mechanically stirred with an overhead stirrer and a polytetrafluoroethylene-coated anchor impeller at 300 rpm to ensure complete dissolution. The solution was then stirred at 10 rpm for 30 min to degas the nitrogen from the dope to ensure nitrogen pockets did not cause a malfunction during solution extrusion.

### Fiber Spinning

Fibers were fabricated using iRJS.[22] Polymer dope (300 mL) was extruded from a Nordson EFD syringe system (EFD 7012436) and 22-Gauge Tapered Tip (EFD 7018298) at 20 psi into the iRJS spinneret spinning at 5,000 rpm. The motor for the iRJS was a Nakanishi E3000 Motor (NR-3080S Spindle, EM-3080J Brushless motor, E3000 Controller, AL-C1204 Airline Kit) with a speed range from 1,000 to 80,000 rpm in 1,000-rpm increments. The spinneret (45.4 mm diameter and two 1-mm diameter orifices) was machined from Hastelloy C276 to resist corrosion form sulfuric acid. The centrifugal force of the spinneret extruded the solution through two 1-mm orifices, through an air gap, and into a 1°C water precipitating

bath. To neutralize the added acid during spinning, we deposited 10 N sodium hydroxide (VWR BDH7247-4) into the bath through a syringe equipped with a conical tip (EFD 7013899, EFD 7016941, EFD 7018298) at 5 psi. The molar rate of 10 N sodium hydroxide deposition matched twice the molar rate of sulfuric acid. As an example, manufacture of 5-g sheets required 500 g of 1% solution to be spun into the bath while 1 L of 10 N NaOH was extruded into the bath for 7 min. The rotating collector pulled fibers in the bath to form the porous network sheet. To remove residual salts and diffuse out any remaining acid after spinning, we washed the sheets in a deionized water bath until the still wet samples had a pH in the range of 5.5–8.5. Sodium hydroxide (10 N) was then added until all residual acid was neutralized. The fibers were then placed in a secondary deionized water wash bath for 2 h. To dry the sheet, we froze the fibers at −80°C for 12 h and placed them in a lyophilizer (SP Scientific FM35EL-85) for 72 h at −80°C and 10–100 mT. If dried under ambient conditions, the evaporation of water would cause the fibers to collapse due to surface tension of the remaining liquid.

### Scanning Electron Microscopy

Scanning electron microscopy (SEM) micrographs were obtained using a Zeiss Supra field-emission scanning electron microscope. Micrographs were gathered using a 5-kV electron source. Single-fiber and sheet samples were secured using carbon tape to bind them to an SEM planchet. To minimize electron buildup in the sample during testing, we applied a 10-nm Pt/Pd coating prior to imaging using an EMS 300T D Dual Head Sputter Coater.

### X-Ray Diffraction

XRD patterns were collected using a Bruker D2 phaser over double the angle of reflection ($2\theta$) range of 5°–90° with a scan speed of 3° $min^{-1}$ and increment of 0.02°. Crystallinity was determined by measuring the area of crystalline versus amorphous peaks.[3]

### Raman Analysis

Raman spectra were collected using a Horiba Multiline Raman Spectrometer with light polarizer, a (red) 633 nm HeNe laser, and an 1,800 g $mm^{-1}$ diffraction grating. Fibers were aligned such that samples appeared vertically in the microscope and placed on a silicon substrate. Laser power was set at 100% (17 mW) for 5 s and averaged between two acquisitions.

### Rheological Testing

Rheological properties of PPTA-$H_2SO_4$ solutions were determined using a TA Instruments Discovery Hybrid 3 Rheometer with cone plate geometry. The cone had a 40-mm diameter, 1.988° angle, and 40-μm truncation gap. A solvent trap was employed to reduce solvent loss during testing. Due to the corrosive properties of sulfuric acid, all materials in contact with the sample were Hastelloy C276. After trimming the sample, the cone was raised and then brought back to the truncation gap, reducing normal force generated during loading. After loading, a 300-s rest time ensured that the sample reached equilibrium. Steady-state sensing was employed over 300 s of testing to ensure the sample reached equilibrium before data were recorded. If subsequent 30-s sample periods were within 5% tolerance of one another, the sample was determined to have reached a steady state and the next point was sampled. To replicate the solution behavior on the iRJS, we probed temperature-dependent properties at 5 Hz, 83 Hz, and 1% strain using a temperature ramp from −10°C to 90°C at a rate of 2.5°C $min^{-1}$. Changes in truncation-gap distance due to thermal expansion were calibrated before testing. Flow-dependent

properties were determined over a shear rate of 0.1–1,000 $s^{-1}$ at 22°C to approximate room temperature and were sampled at 10 points per decade. Strain-dependent properties were determined over a strain of $10^{-2}$% to $10^{2}$% and sampled at 10 points per decade at 22°C, at both 83 Hz and 5 Hz.

### Fiber Tensile Testing

Following ASTM D3822/3822-14, the two ends of a single fiber were adhered to a 150-μm-thick polycarbonate frame (fabricated on a UV laser cutter) using Loctite 770 primer and Loctite 401 adhesives. After evaporative setting for 12 h, the frame was placed into the pneumatic grips of an Instron 5566. Before testing, the frame was cut to allow testing of the fiber only. The fiber was then pulled at a constant strain rate of 10% $min^{-1}$ until it reached failure. After breaking, the fiber was visually inspected to ensure failure occurred in the middle of sample, validating the test methodology. If it did not break between the edges and broke at the ends where the fiber was glued to the frame, the data were not used as the fiber itself was not tested.[33]

### Fragmentation Testing

Ballistic testing measured the strike velocity and residual velocity of a skirted 17-grain (1.1 g), 22-caliber FSP to quantify ballistic resistance of the material in terms of $V_{50}$, the velocity required for a projectile to penetrate a material at a rate of 50% of impacts. Fragmentation testing was performed at the US Army Combat Capabilities Development Command Soldier Center and consisted of a helium gas pressure system to launch the FSP, light gates to measure the $V_1$ and $V_3$ used to calculate the striking velocity ($V_s$) hitting the sample and the residual velocity ($V_r$) leaving the sample, a material mount, and an FSP catcher. Helium gas was used as a charge with variable pressure and therefore potential energy. Upon release, the variable pressure would cause the FSP to travel at a corresponding speed. Light gates measured speed $V_1$ and $V_3$. Calibrating the system allowed for calculations of $V_s$ and $V_r$. The catcher was a metal box with one side open and filled with Kevlar KM2 fabric. Twaron 750D was chosen as a control due to its smaller fiber size of 8 μm versus Kevlar KM2's 10 μm. In addition, Twaron has slightly higher mechanical properties.

### Heat Insulation Testing

Heat insulation was tested using a 600-W heating source (MR Hei-Tec 505-30,000-00) and temperature probes placed on both sides of the samples (Fluke High-Accuracy Thermometer Model 53-II). Changes in temperature with heat flux were used to evaluate the heat conductivity of the samples.[15,16] Samples were normalized using surface area and mass, using samples that were cut to 10 cm by 10 cm in dimension, with a total mass of 5 g.

### Insulation Simulations

Insulation effectiveness of air, Twaron, and *p*AFS was performed in COMSOL Multiphysics 5.3 using the Heat Transfer in Porous Media Physics in a time-dependent study. The heat source was modeled with a 3,500-W heat rate at an initial temperature of 650 K. The air domain was modeled as an ideal gas with an air-flow velocity of 0.03 m $s^{-1}$ in *x* and 0.3 m $s^{-1}$ in *y* with an initial temperature of 273 K. Air-flow velocity was used to match the air-flow conditions of the chemical hood used in the flame testing. An insulator layer of 0.1-cm or 1.75-cm thickness was modeled as an ideal gas of air, porous material of Twaron, or porous material of *p*AFS. Heat conductivity for Twaron and *p*AFS was derived during heat-insulation testing. Heat capacity value of 1,400 J $(kg\ K)^{-1}$ based on literature was used for Twaron and *p*AFS. Twaron density was modeled as 480 kg $m^{-3}$ and volume fraction as 0.33. *p*AFS density was

modeled as 51 kg $m^{-3}$ and volume fraction as 0.035 based on experimental measurements. The heat sink was modeled as water. Unless otherwise stated, the initial temperature of the materials was 273 K. Mesh size was set as normal and the solver was solved from 0 to 2,400 s in 1-s increments.

### Flame Testing

Equivalent masses of *p*AFS and Twaron sheets were used to determine their insulation properties. Gelatin astronaut models (GAMs) were used during testing to provide a visual representation of the heat-insulation capabilities of each material, created using a 3:2 (w/w) ratio of deionized water to gel strength 300 Type A porcine gelatin (Sigma-Aldrich, USA), specifically 120 g of deionized water and 80 g of gelatin powder. After mixing, the solution was left to bloom for 10–15 min before being placed in an 80°C water bath and stirred until completely dissolved. Fifteen drops of red food coloring and 1 drop of blue food coloring were then added for visual appeal. The mixture was then removed from heat, poured into a mold, and placed in a refrigerator for a minimum of 12 h for the gelatin to set. When removed from the mold, the GAM was placed in the freezer to prevent contamination. Before insulation testing, the GAMs were thawed from the freezer. A blowtorch (Coleman Propane Fuel Tank, Bernzomatic TS8000, SEARZALL) was then placed at a distance of 10 cm from the astronaut for three trials consisting of no protection, insulation by Twaron sheets, and insulation by *p*AFS. When insulation was present, the sheets were positioned at a distance of 10 cm between the blowtorch and the GAM. The blowtorch temperature was 350°C $\pm$ 25°C. Flame testing occurred in a chemical hood to contain any fire outbreaks. As material can be melted away over time or the fabric layers could catch fire, the torch was manually held at this distance. Photo images were recorded every five seconds until half of the GAM melted or 35 min elapsed.

### Statistical Analysis and Data Representation

To determine statistical significance, we analyzed datasets to determine whether they were normally distributed. If a dataset had an $n > 30$ and skewness in the range of −0.5 to 0.5, the dataset was assumed to have a normal distribution. A normally distributed group of data was then tested using a one-way ANOVA and a post hoc Tukey method. If datasets had an $n < 30$ or a skewness outside the range of −0.5 to 0.5, the dataset was not assumed to be normally distributed. A dataset with an unknown distribution was tested using ANOVA on ranks and a post hoc Mann-Whitney. A p value of $<0.05$ was considered to be statistically significant (see Table S1). This procedure was performed in SigmaPlot 13. Box plots with overlaying data points were used to fairly depict data. The middle line of a box represents the median (M), the top of a box represents the 75$^{th}$ quartile ($Q_{75}$), the bottom of a box represents the 25$^{th}$ quartile ($Q_{25}$), the box represents the interquartile range (IQR), the top whisker represents M + 1.5 IQR, and the bottom whisker represents M – 1.5 IQR.

## SUPPLEMENTAL INFORMATION

Supplemental Information can be found online at https://doi.org/10.1016/j.matt.2020.06.001.

## ACKNOWLEDGMENTS

We thank Dr. Luke MacQueen and Dr. Christopher Doona for reviewing the manuscript, Daniel Drennan for optimizing Raman spectroscopy settings, and Grace Mathews and Michael Rosnach for figure illustrations. This work was performed in

part at the Center for Nanoscale Systems (CNS), a member of the National Nanotechnology Infrastructure Network, which is supported by the National Science Foundation under NSF award no. ECS-0335765. CNS is part of Harvard University. We thank the Harvard Materials Research Science and Engineering Center under the National Science Foundation, United States award number DMR-1420570 for funding and access to rheological tools, and the Harvard University, United States Physical Sciences & Engineering Accelerator Fund. We are grateful for the assistance of Dr. Shao-Liang Zheng with the X-ray analysis. We would like to thank the Wyss Institute of Biologically Inspired Engineering at Harvard University for providing access to the Instron for mechanical testing.

## AUTHOR CONTRIBUTIONS

G.M.G., J.F.Z., F.J.B., and K.K.P. conceived and designed the study. G.M.G., J.W., J.S., K.S., and S.A.F. performed and analyzed fragmentation testing data. G.M.G., J.L.P., F.W.Z., V.M.L., and L.C. manufactured and characterized *p*AFS and control materials. G.M.G. performed and analyzed rheological experiments and data. G.M.G., J.F.Z., F.J.B., and K.K.P. wrote and edited the manuscript.

## DECLARATION OF INTERESTS

Harvard University owns the rights to US Patent 10519569, "Immersed rotary jet-spinning devices (IRJS) and uses thereof," which was used in this work.

Received: February 19, 2020
Revised: April 15, 2020
Accepted: May 29, 2020
Published: June 29, 2020

## REFERENCES

1. Young, A. (2009). Spacesuits: The Smithsonian National Air and Space Museum Collection (PowerHouse Books).
2. McQuaid, M. (2005). Extreme Textiles : Designing for High Performance (Princeton Architectural Press).
3. Yang, H.H. (1993). Kevlar Aramid Fiber (John Wiley & Sons).
4. Tanner, D., Fitzgerald, J.A., and Phillips, B.R. (1989). The Kevlar story—an advanced materials case study. Adv. Mater. *5*, 151–156.
5. Bhat, G. (2016). Structure and Properties of High-Performance Fibers (Elsevier Science).
6. Chae, H.G., and Kumar, S. (2006). Rigid-rod polymeric fibers. J. Appl. Polym. Sci. *100*, 791–802.
7. Bourbigot, S., and Flambard, X. (2002). Heat resistance and flammability of high performance fibres: a review. Fire Mater. *26*, 155–168.
8. Goto, T., Iida, M., Tan, H., Liu, C., Mayumi, K., Maeda, R., Kitahara, K., Hatakeyama, K., Ito, T., Shimizu, Y., et al. (2018). Thermally conductive tough flexible elastomers as composite of slide-ring materials and surface modified boron nitride particles via plasma in solution. Appl. Phys. Lett. *112*, 101901.
9. Pabst, W., and Gregorová, E. (2015). Critical Assessment 18: elastic and thermal properties of porous materials—rigorous bounds and cross-property relations. Mater. Sci. Technol. *31*, 1801–1808.
10. Wang, X., Ho, V., Segalman, R., and Cahill, D.G. (2013). Thermal conductivity of high-modulus polymer fibers. Macromolecules *46*, 4937–4943.
11. Kim, P.K., Chang, C., and Hsu, S.L. (1986). Normal vibrational analysis of a rigid rod polymer: poly(p-phenylene terephthalamide). Polymer *27*, 34–46.
12. Yang, M., Cao, K., Sui, L., Qi, Y., Zhu, J., Waas, A., Arruda, E.M., Kieffer, J., Thouless, M.D., and Kotov, N.A. (2011). Dispersions of aramid nanofibers: a new nanoscale building block. ACS Nano *5*, 6945–6954.
13. Cao, K., Siepermann, C.P., Yang, M., Waas, A.M., Kotov, N.A., Thouless, M.D., and Arruda, E.M. (2013). Reactive aramid nanostructures as high-performance polymeric building blocks for advanced composites. Adv. Funct. Mater. *23*, 2072–2080.
14. Yeager, M.P., Hoffman, C.M., Xia, Z., and Trexler, M.M. (2016). Method for the synthesis of para-aramid nanofibers. J. Appl. Polym. Sci. *133*, 44082.
15. Lyu, J., Liu, Z., Wu, X., Li, G., Fang, D., and Zhang, X. (2019). Nanofibrous kevlar aerogel films and their phase-change composites for highly efficient infrared stealth. ACS Nano *13*, 2236–2245.
16. Liu, Z., Lyu, J., Fang, D., and Zhang, X. (2019). Nanofibrous kevlar aerogel threads for thermal insulation in harsh environments. ACS Nano *13*, 5703–5711.
17. Roenbeck, M.R., Sandoz-Rosado, E.J., Cline, J., Wu, V., Moy, P., Afshari, M., Reichert, D., Lustig, S.R., and Strawhecker, K.E. (2017). Probing the internal structures of Kevlar® fibers and their impacts on mechanical performance. Polymer *128*, 200–210.
18. Roenbeck, M.R., Cline, J., Wu, V., Afshari, M., Kellner, S., Martin, P., Londono, J.D., Clinger, L.E., Reichert, D., Lustig, S.R., et al. (2019). Structure-property relationships of aramid fibers via X-ray scattering and atomic force microscopy. J. Mater. Sci. *54*, 6668–6683.
19. Li, G., Zhu, M., Gong, W., Du, R., Eychmüller, A., Li, T., Lv, W., and Zhang, X. (2019). Boron nitride aerogels with super-flexibility ranging from liquid nitrogen temperature to 1000 °C. Adv. Funct. Mater. *29*, 1–7.
20. Hu, P., Lyu, J., Fu, C., Gong, W.B., Liao, J., Lu, W., Chen, Y., and Zhang, X. (2020). Multifunctional aramid nanofiber/carbon nanotube hybrid aerogel films. ACS Nano *14*, 688–697.
21. Li, J., Wang, J., Wang, W., and Zhang, X. (2019). Symbiotic aerogel fibers made via in-situ gelation of aramid nanofibers with polyamidoxime for uranium extraction. Molecules *24*, 1821–1835.

22. Gonzalez, G.M., MacQueen, L.A., Lind, J.U., Fitzgibbons, S.A., Chantre, C.O., Huggler, I., Golecki, H.M., Goss, J.A., and Parker, K.K. (2017). Production of synthetic, para-aramid and biopolymer nanofibers by immersion rotary jet-spinning. Macromol. Mater. Eng. *302*, 1600365.

23. Tanner, R.I. (2005). A theory of die-swell revisited. J. Nonnewton. Fluid Mech. *129*, 85–87.

24. Han, W., Zhao, T., and Wang, X. (2015). Study of first normal stress difference of poly(p-phenylene terephthalamide) in sulfuric acid. Polymer *57*, 150–156.

25. Karger-Kocsis, J. (1999). Polypropylene: An A-Z Reference (Springer).

26. Kharchenko, S.B., Douglas, J.F., Obrzut, J., Grulke, E.A., and Migler, K.B. (2004). Flow-induced properties of nanotube-filled polymer materials. Nat. Mater. *3*, 564–568.

27. Mewis, J. (1990). An introduction to rheology. Powder Technol. *61*, 295.

28. Baird, D.G. (1980). Rheological properties of liquid crystalline solutions of poly- p -phenyleneterphthalamide in sulfuric acid. J. Rheol. *24*, 465–482.

29. Koopmans, R., and Molenaar, J. (1998). The "Sharkskin Effect" in polymer extrusion. Polym. Eng. Sci. *38*, 101–107.

30. Penn, L., and Milanovich, F. (1979). Raman spectroscopy of Kevlar 49 fibre. Polymer *20*, 31–36.

31. Cunniff, P.M. (1999). Dimensionless parameters for optimization of textile-based body armor systems. In Proceedings of the 18th International Symposium on Ballistics, W.G. Reinecke, ed. (Technomic Publishing Co. Inc.), pp. 1303–1310.

32. Stephan, K., and Laesecke, A. (1985). The thermal conductivity of fluid air. J. Phys. Chem. Ref. Data *14*, 227–234.

33. Wang, H.X., Hazell, P.J., Shankar, K., Morozov, E.V., and Escobedo, J.P. (2015). The effectiveness of combined gripping method in tensile testing of UHMWPE single yarn. IOP Conf. Ser. Mater. Sci. Eng. *87*, https://doi.org/10.1088/1757-899X/87/1/012109.

**Matter, Volume *3***

## Supplemental Information

# *para*-Aramid Fiber Sheets for Simultaneous Mechanical and Thermal Protection in Extreme Environments

**Grant M. Gonzalez, Janet Ward, John Song, Kathleen Swana, Stephen A. Fossey, Jesse L. Palmer, Felita W. Zhang, Veronica M. Lucian, Luca Cera, John F. Zimmerman, F. John Burpo, and Kevin Kit Parker**

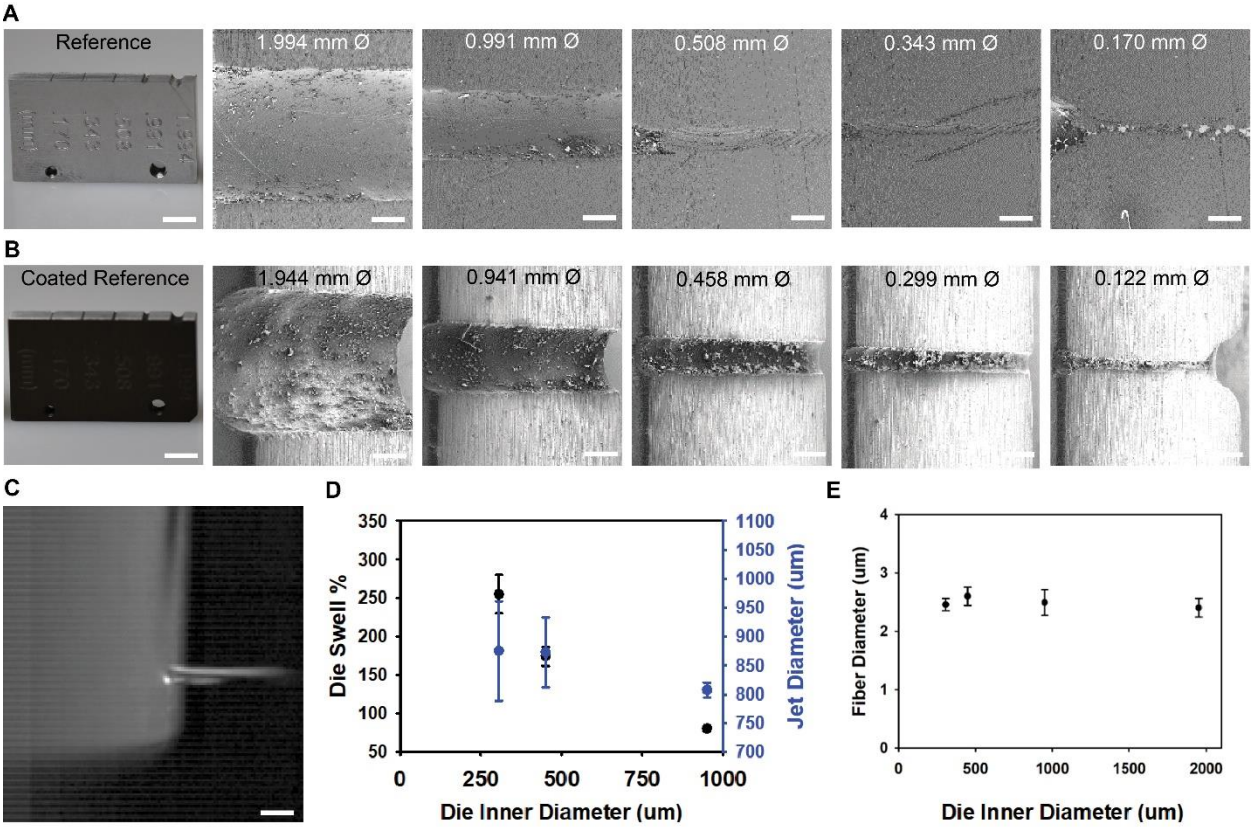


Figure S1: Affect of Die Diamter on Fiber Diameter. A) Reference die diameters can be milled with different sizes from 1.994 mm to .170 mm (scale bar = 1 mm) and further reduced B) using an anodizing hard coat to have a range of 1.944 mm to .122 mm (scale bar = 1 mm). C) As seen in a test case of Hyalronic acid-water solutions, the jet diamter of the spinneret (scale bar = 2 mm) D) does not change with die diameter due to normal force generation. E) Due to the die swelling, hyallronic acid fibers made from different die sizes have the same diameter. Hyallronic acid-water solutions and PPTA-sulfuric acid solutions tested were both dillute, isotropic solutions that have normal force increase with increasing shear rate.

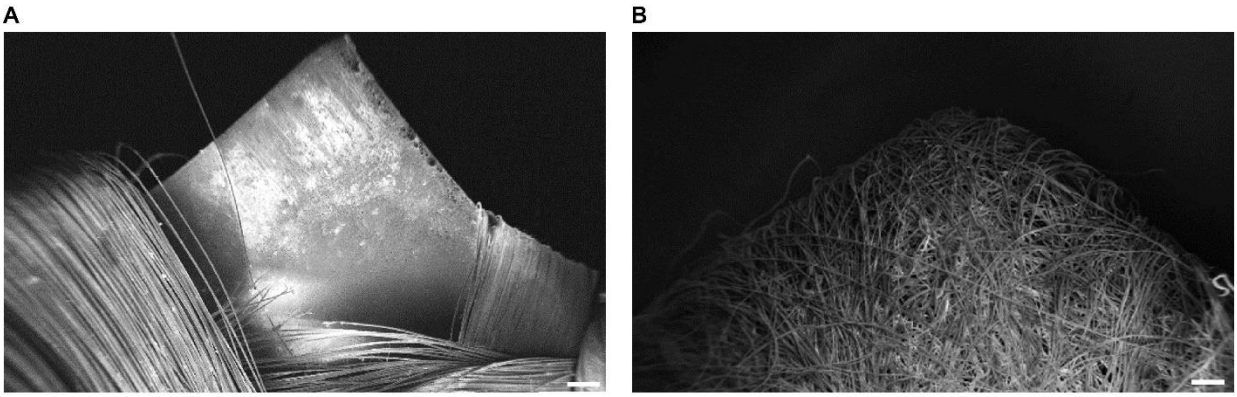


Figure S2: Fiber Sheet Puncture Resitance. A) The weave of commercial para-aramids allow for puncture between the individual woven pleats while the B) smaller fiber size and non-woven nature of the *p*AFS provide greater resistance to puncture (scale bars = 250 µm).

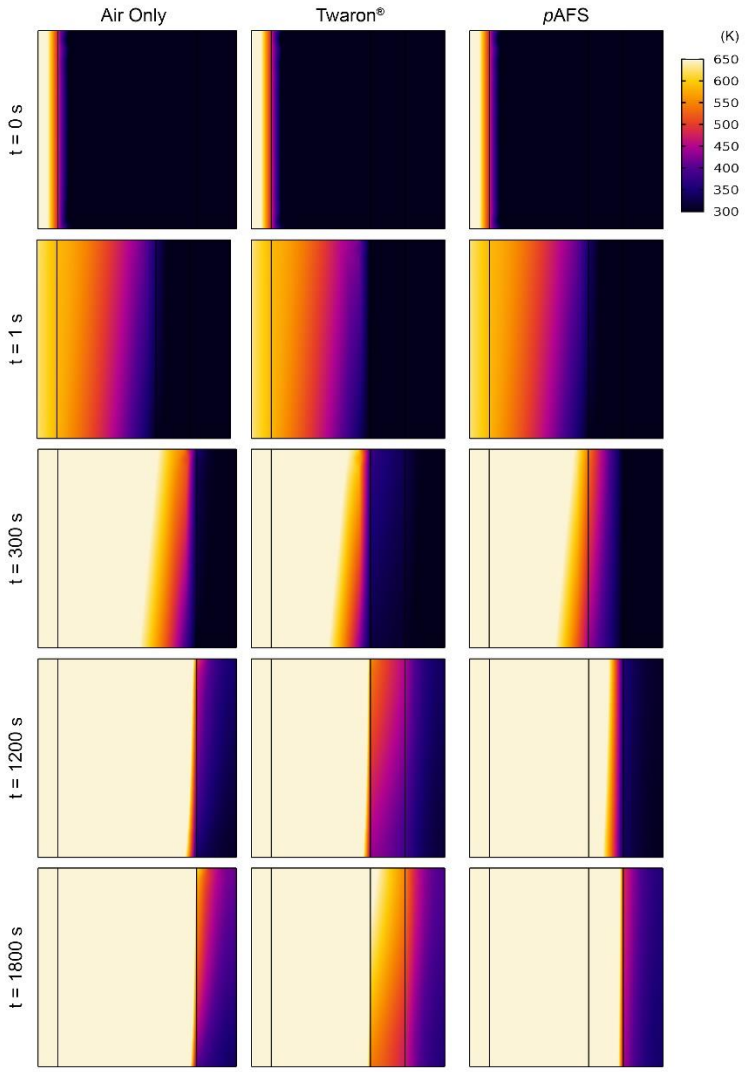


Figure S3: Insulation simulation with a 5 cm air gap and 1 cm insolator material of air, a commercail *p*-aramid, or *p*AFS.

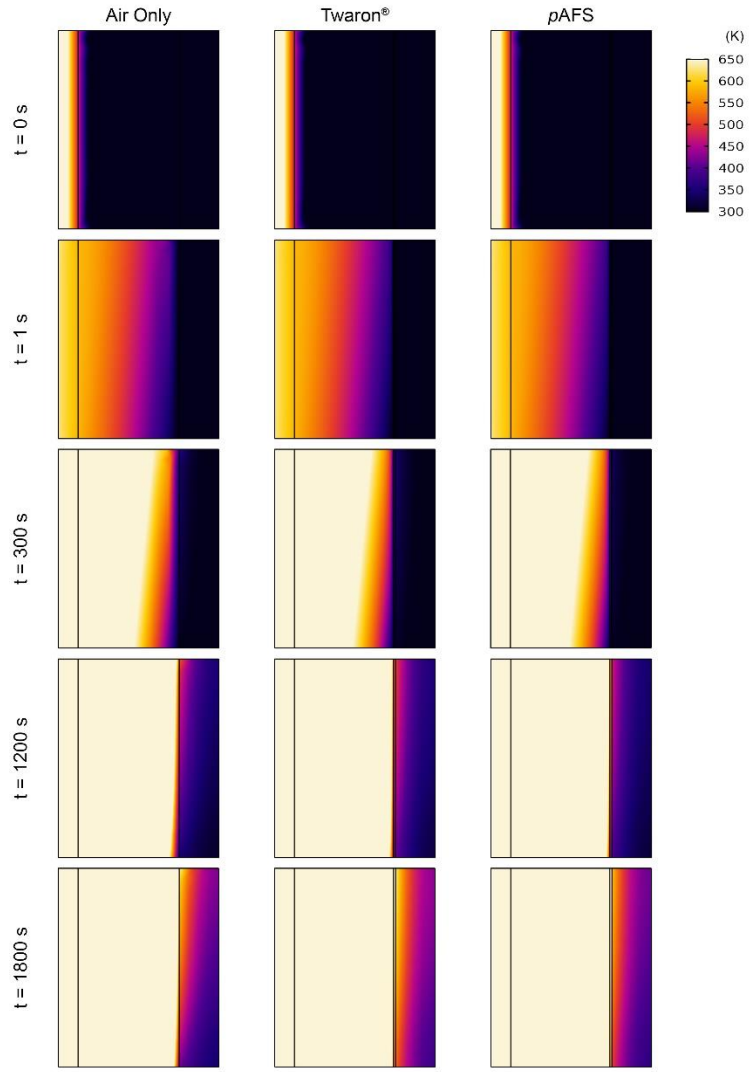


Figure S4: Insulation simulation with a 5 cm air gap and 1 mm insolator material of air, a commercail *p*-aramid, or *p*AFS.

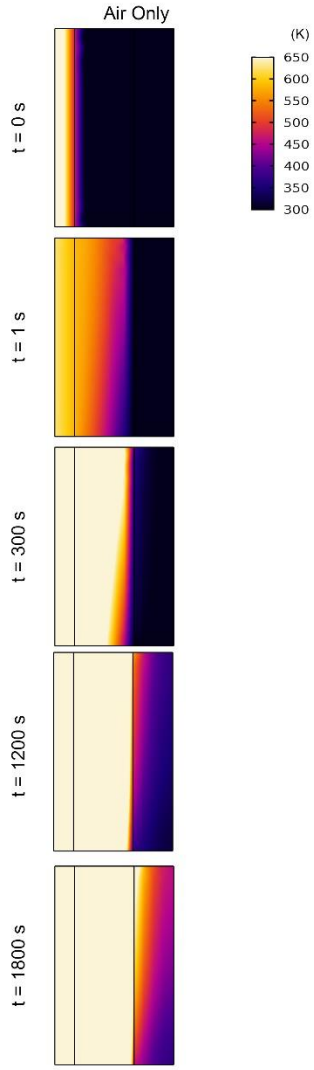


Figure S5: Insulation simulation with a 3 cm air gap only.

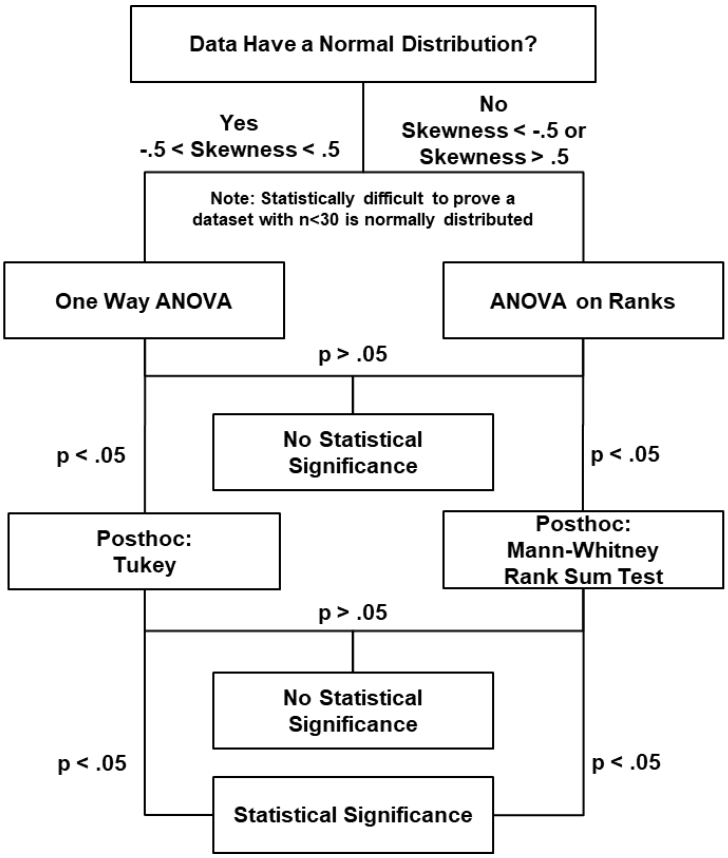


Table S1: Statistical Flow Diagram for Determining the Method to Use to Determine Statistical Significance.